

UNCLASSIFIED

## MODELOCKED-LASER LASER RADAR PERFORMANCE IN THE DETECTION OF TMD AND NMD TARGETS

Douglas G. Youmans  
Schafer Corp.  
321 Billerica Rd.  
Chelmsford, MA 01890

Rodney Robertson  
USASSDC  
P.O. Box 1500  
Huntsville, AL 35807

### Abstract

Ultra-compact mode-locked CO<sub>2</sub> lasers and mode-locked Nd:fiber lasers are being developed for Theater Missile Defense (TMD) and National Missile Defense (NMD) applications. These lasers produce a coherent train of narrow pulses which may be used in a coherent laser radar (ladar) to form an image of a possible target. The distance to the target is irrelevant as long as there is enough received energy. These images are known as "range-Doppler," "range-resolved Doppler," or "inverse synthetic aperture radar (ISAR)" images. The down-range image resolution is given by the micro-pulse width multiplied by  $c/2$ , and the image Doppler resolution is given by the reciprocal total pulse length consisting of many hundreds of micro-pulses. In this paper we briefly review previous work on the target range-Doppler image features which are useful for target discrimination, and then we examine the detection of the target under low signal conditions given passive sensor or radar handover range and velocity information which contains errors. A Gaussian-mode radiometry analysis is presented, the range-Doppler image formation process is reviewed, and the effects of target speckle, pointing errors, and atmospheric turbulence are discussed. A metric for determining a "target detection," under these low-signal initial conditions, is proposed.

### 1.0 Introduction

Under the Discriminating Interceptor Technology Program (DITP) and Advanced Sensors Technology Program (ASTP) at BMDO<sup>1,2</sup>, ultra-compact mode-locked CO<sub>2</sub> and mode-locked Nd:fiber ladars are being developed which, when used in conjunction

with passive sensors or radar, will enhance the discrimination robustness of future interceptors. Missile seeker technology development is the emphasis of DITP, and surveillance sensor technology is the focus of ASTP. Combining a ladar and passive sensor outputs will increase the number of target features observed due to the complementary nature of the target signatures measured. For example, ladar measurements of range-resolved intensity and velocity are not directly obtainable with passive sensor measurements. Likewise, in conjunction with a radar, the ladar provides precision target angular information as well as more precise range, Doppler, and range-resolved Doppler measurements.

The mode-locked lasers under development<sup>1,2</sup> produce a train of coherent narrow pulses, or "micro-pulses," of pulsewidths from 1.3 ns to 2.9 ns. This corresponds to a down-range resolution of from 20 cm (NMD) to 44 cm (TMD). Also, the frequency of the CO<sub>2</sub> laser is 28,300 GHz (10.6  $\mu$ m) for exo-atmospheric operation or 26,900 GHz (11.15  $\mu$ m isotopic CO<sub>2</sub>) for endo-atmospheric operation. The frequency of the Nd:fiber laser is 283,000 GHz (1.06  $\mu$ m). Since target velocity resolution is approximately  $\lambda/2T_{\text{waveform}}$ , we see that the velocity resolution is about 3,000 or 30,000 times higher than that of X-band radar. (Or, the same measurement can be done in 1/3,000th to 1/30,000th of the time.) The target image Doppler resolution is also determined by the reciprocal total "macro-pulse" time consisting of many hundreds of micro-pulses. Consequently, it is possible to form a precision target range-resolved Doppler image in real time which is useful for target discrimination. In this paper we will concentrate on the CO<sub>2</sub> ladar systems.

Approved for Public Release;  
Distribution is unlimited.

19970912 118

## 2.0 Image Feature Extraction for Discrimination

Previous papers<sup>3,5</sup> have examined feature extraction from ladar range-resolved Doppler images for target discrimination. Two range-Doppler images<sup>4</sup> of cones, taken at the U.S. Army AMOR facility, are shown in **Figure 1** for cone aspect angles of 15° and 30°. Target surface produced laser light speckle, due to the rough surface with respect to  $\lambda$ , can be seen in the images. This speckle effect can be reduced by a non-coherent summation of consecutive range-Doppler images, although it is difficult to maintain perfect range and frequency registration for precise summing and it requires additional time. The target features that can be estimated<sup>3,4</sup> from the range-Doppler image include: target length, diameter, spin rate, precession rate, precession half-angle, center of mass location, total cross-section, range-resolved cross-section, cross-section fluctuation statistics in time and frequency domains, and aspect angle variations of total and resolved cross-section. A sub-set of these estimated parameters has been found<sup>4</sup> to be adequate for RV and decoy discrimination.

## 3.0 Gaussian Mode Coherent Ladar Analysis

The ladar carrier-to-noise ratio (CNR), or signal-power to local-oscillator-noise-power ratio, is determined by integrating the transmitted laser beam and the back-propagated-local-oscillator laser beam (including turbulence effects on both beams) over the surface of the unresolved target. This treatment follows the work of Frehlich<sup>6</sup>, also known as the "beam-overlap" technique. We propagate the laser beam from the laser to the transmitting aperture and then out to the target, and we also back-propagate the LO beam incident on the detector (including clipping), back out to the receiving aperture (more clipping), and then back out to the target. This is denoted as the BPLO mode. The two modes are then integrated over the target surface where a diffuse target scattering function can be used to simplify the complicated integrals. This simplification results in a CNR given by

$$CNR(t) = \frac{\eta \lambda^2 e^{-2 \int \alpha dz}}{h \nu B P_{LO \det}} \times \int_{-\infty}^{\infty} \rho(\vec{p}) \langle I_T(\vec{p}, R, t-R/c) \rangle \langle I_{BPLO}(\vec{p}, R) \rangle d\vec{p} \quad (1)$$

where  $I_T$  and  $I_{BPLO}$  are the laser irradiance at the

transmitter aperture propagated out to the target and the back-propagated-local-oscillator beam irradiance on the target, excluding the atmospheric extinction. The brackets indicate averaging over atmospheric turbulence effects. "B" is the electrical bandwidth assumed to be flat-top and subtending all of the received signal frequencies and yet no more than necessary of the local oscillator noise caused by  $P_{LO}$  incident on the detector. " $\rho$ " is the unresolved target scattering function in  $m^2/sr$  described below, and " $\eta$ " is the detector quantum efficiency, 0.5 for  $CO_2$  and 0.85 for Nd:fiber. " $\alpha$ " is the atmospheric extinction coefficient often taken to be that of a mid-latitude summer atmosphere with rural aerosol with 23 km visibility at low altitudes and background-plus-aged-volcanic stratospheric aerosols. The integral over  $\alpha$  is computed in spherical-shell layers along the path of the laser mode and the backscattered speckle-pattern return. (Note,  $\alpha$  is zeroed for exo-atmospheric operation.) Higher-order terms<sup>6</sup> in the integrand of (1) result in an occasional +3dB "backscatter enhancement" which is neglected here.

The transmitted and BPLO mode irradiances at a distance R from the ladar are both Gaussian:

$$\langle I_T(\vec{p}; R) \rangle = \frac{2 P_{laser}}{\pi \omega^2(R)} t_t S_{trn} e^{-\int \alpha dz} \exp(-2 p^2 / \omega^2(R))^{(2)}$$

in good agreement with Technology Development Corp., Hughes, and Textron Systems Div. mode-locked laser measurements. We assume optical train transmissions,  $t_t$  and  $t_r$ , of 0.7 each. The laser mode  $1/e^2$  irradiance radius at range R is given by

$$\omega^2(R) = \omega_o^2 + \left( \frac{\lambda R}{\pi \omega_o S_{opt}} \right)^2 + \left( \frac{\lambda R}{\pi \rho_o(R)} \right)^2 \quad (3)$$

which includes the effect of **atmospheric turbulence** on the **average** irradiance<sup>6</sup> through  $\rho_o(R)$ .  $\omega_o$  is the  $1/e^2$  irradiance beam waist radius located near the aperture of the telescope. The optical train and boundary layer aberration effects produced Strehl ratio,  $S_{opt}$ , is assumed to be negligible, equal to 1.0 here. The transverse coherence distance  $\rho_o(R)$  given by<sup>6</sup>:

$$\rho_o(R) = \left( 2.91 k^2 \int_0^R dz C_n^2(z) (1 - z/R)^{5/3} \right)^{-3/5} \quad (4)$$

where  $z = 0$  corresponds to the ladar transmitting / receiving aperture. The quantity  $C_n^2(h)$  is the "refractive index structure coefficient" vs altitude. The Hufnagle-Valley 5/7 and clear one night models

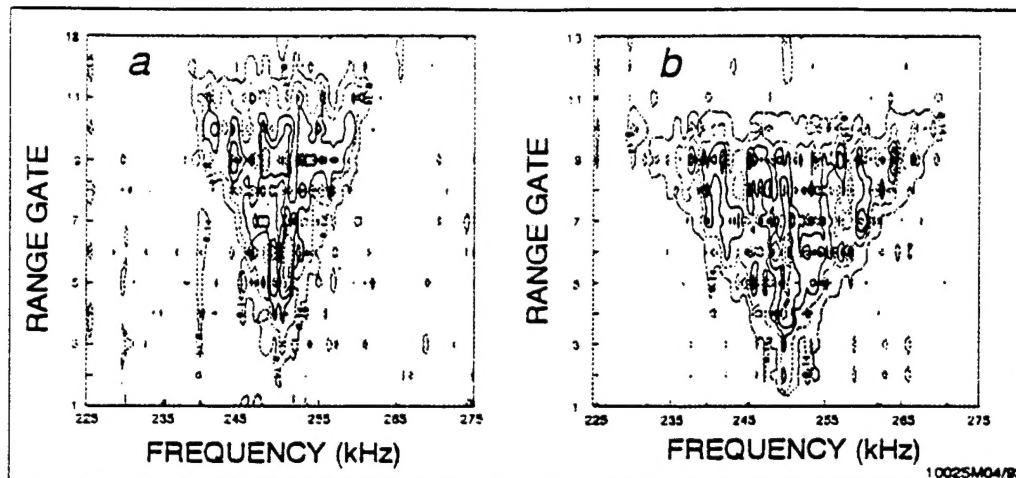


Figure 1. AMOR range-Doppler image<sup>4</sup> of a spinning cone at 15° and 30°.

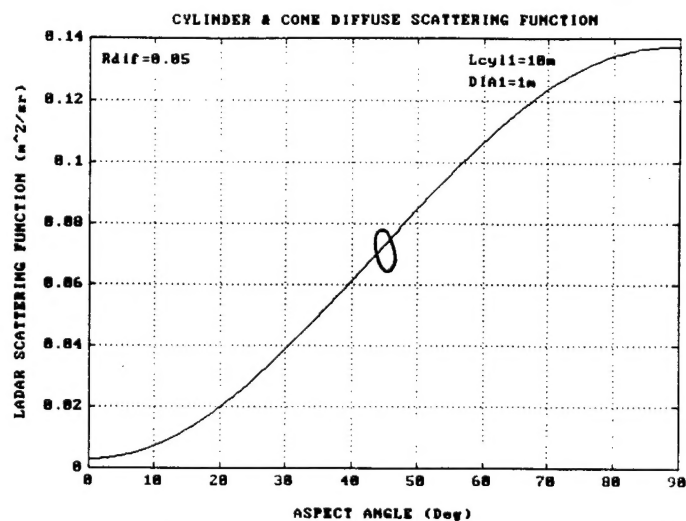


Figure 2. Cross-section ( $\text{m}^2/\text{sr}$ ) of a 10 m x 1 m cylinder with 2 m conical tip, 5% diffuse reflectivity.

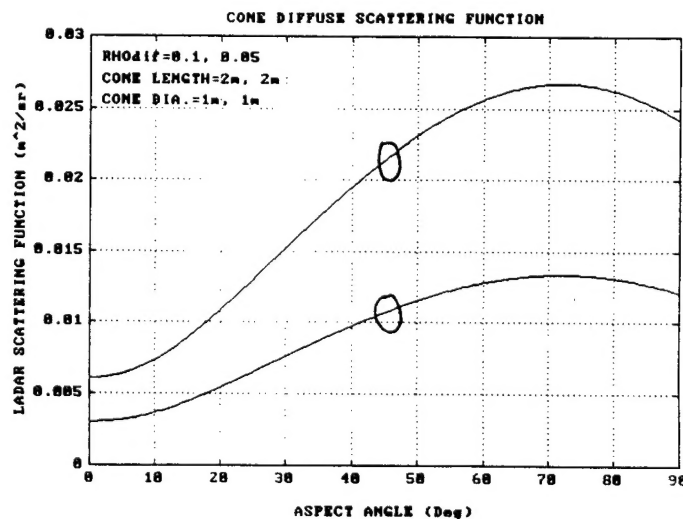


Figure 3. Cross-section ( $\text{m}^2/\text{sr}$ ) of a 2 m x 1 m cone, 10% and 5% diffuse reflectivity.

are often used. (For exo-atmospheric ladars,  $C_n^2 = 0$  and  $\rho_o$  is infinite.) We see that the average effect of atmospheric turbulence is to spread the transmitted and BPLO modes and thereby decrease the received signal strength. At  $\text{CO}_2$  laser wavelengths this effect is usually only a few percent unless the TMD target is still close to the ground.

### 3.1 Gaussian Mode Strehl Ratios

The laser mode Strehl ratio,  $S_{\text{tm}}$ , is reduced by telescope clipping and central obscuration. Degnan and Klein<sup>7</sup> have shown that for a given aperture diameter,  $d_{\text{rec}} = 25$  cm here, the Strehl ratio is

$$S_{\text{tm}}|_{d_{\text{rec}}} = (\exp(-\alpha^2\gamma^2) - \exp(-\alpha^2))/\alpha^2 \quad (5)$$

where

$\alpha$  = clear aperture radius /  $\omega_o$  ( $= 1.12$  for maximum irradiance @  $\gamma = 0$ )

$\gamma$  = linear obscuration ratio

$\omega_o = 12.5$  cm /  $1.12 = 11.125$  cm for maximum irradiance

full angle =  $4\lambda/(\pi 2\omega_o) = 63.8 \mu\text{r}$  @  $11.15 \mu\text{m}$   
@  $1/e^2$  irradiance

Yura<sup>8</sup> gave identical results for  $\gamma = 0$ . However, to get the correct "Strehl ratio" for use in equation (2), we would ordinarily solve equation (5) for the optimum  $\alpha$ , and then substitute this value of  $\alpha$  into the **Strehl ratio equation for a given  $\omega_o$**  (which is the correct  $S_{\text{tm}}$ ):

$$S_{\text{tm}}|_{\omega_o} = (\exp(-\alpha^2\gamma^2) - \exp(-\alpha^2))^2 \quad (6)$$

This is because the far-field irradiance distribution in the absence of aperture clipping and obscuration, in the definition of a Strehl ratio, is a function of  $\omega_o$  only. For **maximum on axis irradiance**,  $S_{\text{tm}} = S_{\text{BPLO}} = 0.51$  from equation (6) for  $\text{CO}_2$ . At  $1.06 \mu\text{m}$  and a  $50 \mu\text{r}$  full angle divergence, these terms are almost 1.

### 3.2 Pointing Bias and Jitter Effects

Yura<sup>9</sup> has developed an approximation for the average decrease in received irradiance due to pointing jitter and bias errors for direct detection. For **coherent** detection the mixing efficiency is also degraded by an off-axis target source, when there is a pointing error, due to both a decrease in transmitted irradiance and BPLO irradiance, as indicated in equations (1) and (2) above. Therefore, we define a Gaussian transmitted intensity times an off-axis mixing efficiency degradation due to a decrease in the BPLO irradiance as

$$I(\theta) = I_o \exp(-\theta^2/2\theta_o^2) \exp(-\theta^2/2\theta_{pt}^2) \quad (7)$$

and repeat Yura's calculation to find the irradiance probability density function

$$p_{pt}(I|a,b) = \frac{a^2}{2I_o} e^{-a^2b^{1/2}} \left(\frac{I}{I_o}\right)^{a^2/2-1} J_o(a^2b[\ln(I/I_o)]^{1/2}) \quad (8)$$

where  $a$  and  $b$  are defined w.r.t. the Gaussian mode

$$\theta_o = \frac{\lambda}{2\pi\omega_o} = \frac{\theta_{1/e^2}}{2}, \quad a = \frac{\theta_o}{\sigma_j}, \quad b = \frac{\theta_{pt}}{\theta_o} \quad (9)$$

Normalizing  $I$  by  $I_o$  to define  $I_n$ , we also have

$$p_{pt}(I_n|a,b) = \frac{a^2}{2} e^{-a^2b^{1/2}} I_n^{a^2/2-1} J_o(a^2b[\ln(I_n)]^{1/2}) \quad (10)$$

The average **coherent** detection intensity and mixing-efficiency-product,  $\langle I_n \rangle$ , can then be computed for various  $\sigma_j$  and  $\theta_{pt}$ :

$$\alpha_{coh} = \left(\frac{a^2}{a^2+2}\right) \exp\left(\frac{-b^2a^2}{a^2+2}\right) \approx \langle I_n \rangle \quad (11)$$

where  $\alpha_{coh}$  is Yura's " $\alpha$ " parameter approximation for **coherent** detection.

The ladar fast steering mirror and slow steering mirror will have bias and jitter errors. In addition, the commanded azimuth and elevation pointing angles will also have bias and jitter errors. We assume **3  $\mu\text{r}$  of bias, 10  $\mu\text{r}$  of jitter**, and  $\omega_o = 11.125$  cm, and we find  $\alpha_{coh} = 0.55$  in this analysis.

### 3.3 Target Cross-section Models

For the TMD target we will assume that the target is a **cylinder 10 m long and 1 m in diameter with a 2 m long conical tip** having a diffuse reflectivity coefficient of 5% at  $11.15 \mu\text{m}$ . In **Figure 2** is the cylinder+cone cross-section<sup>10</sup> in  $\text{m}^2/\text{sr}$  vs aspect angle. The retro-reflective and glint components are omitted because they are generally negligible, with respect to the diffuse component, except near  $90^\circ$  aspect. We also choose this cylinder to be at  $45^\circ$  aspect angle, thus, it is 7 m in depth. Each TMD ladar micro-pulse is 2.9 ns or 87 cm in length. When 50% of the target surface scattering points within the micro-pulse are replaced, we have a new speckle source. Thus, every 87 cm/2 produces a new speckle source, and the missile cross-section may be divided among about 14 nearly independent target down-range coherent return cells. The cross-section per independent range cell is then taken as

$$\sigma_{\text{target}} \approx 0.074 (\text{m}^2/\text{sr}) / 14 \equiv \rho_{\text{tar}} A_{\text{tar}} / \pi \quad (12)$$

where the  $(\rho A/\pi)$  indicates an area x reflectivity / sr for clarity. To detect a target, only one or more of the down-range cells must exceed a threshold. (At larger aspect angles near  $90^\circ$ , the total cross-section goes up, and the number of range coherence cells approaches one, greatly increasing the CNR per range cell.)

The NMD target is taken to be a **2 m long, 1 m diameter cone** with 5% diffuse reflectivity at  $10.6 \mu\text{m}$  (and 10% diffuse reflectivity at  $1.06 \mu\text{m}$ ) as shown in **Figure 3**. The micro-pulses are taken to 1.3 ns long for 20 cm range resolution, thus the cone at  $45^\circ$  produces roughly 7 independent range cell returns. Again, we neglect the retro-reflective and glint components.

### 3.4 Unresolved Target CNR Model

We can now evaluate the overlap integral of equation (1) assuming a **delta-function** for the unresolved target angular (transverse) subtense

$$\rho(\vec{p}, \vec{a}) = \frac{\rho_{tar}}{\pi} A_{tar} \delta(|\vec{p} - \vec{a}|) \quad (m^2/sr) \quad (13)$$

and assuming some pointing error offset "a" from the optical axis of the LADAR. Assuming this delta-function target model, we get using (1), (2), and (13)

$$CNR(t) = \frac{P_{laser}(t-2R/c) \eta_t t_r e^{-2\int \alpha dz}}{h\nu B} \times \quad (14)$$

$$\eta_s \eta_\phi(R) \left( \frac{\rho_{tar} A_{tar}}{\pi} \right) \frac{4\lambda^2}{\pi^2 \omega^4(R)} \exp\left(\frac{-4a^2}{\omega^2(R)}\right) \alpha_{COH}$$

for aligned transmitter and BPLO modes. We have defined a "system efficiency" as

$$\eta_s = 0.83 S_{tm} S_{BPLO} \quad (15)$$

where  $S_{tm}$  and  $S_{BPLO}$  are from Section 3.1, and 0.83 is the best mixing efficiency<sup>7</sup> for a Gaussian LO mode and the Airy disk with  $\gamma = 0$ . We have also included an interference fringe-contrast-ratio degradation term,  $\eta_\phi(R)$ , to account for the decrease in fringe contrast, versus round-trip delay time, due to phase-noise within the LO laser source. In this analysis we set this term to 1.0 corresponding to a perfect LO laser.

### 4.0 Classical Receiver-Operating-Characteristic

In heterodyne detection, the detector output is bandpass filtered around an intermediate frequency (IF) produced by mixing the backscattered light signal with the LO laser to maximize CNR following equation (1). For a pure speckle target both the

signal and LO noise are Gaussian random processes. Following envelope detection<sup>11</sup> theory, the rectified and low-pass filtered signal and LO noise voltages are Rayleigh distributed. The probability of a false alarm is then the integral from some threshold voltage to infinity over the output voltage probability density function (PDF) in the absence of signal:

$$P_{FA} = \int_{v_i}^{\infty} \frac{v}{\sigma_{Lo}^2} \exp\left(\frac{-v^2}{2\sigma_{Lo}^2}\right) dv = \exp(-v_i^2/2\sigma_{Lo}^2) \quad (16)$$

Likewise, the probability of detection is the integral from the same threshold voltage over the output PDF in the presence of both noise and signal:

$$P_D = \exp(-v_i^2/2(\sigma_{Lo}^2 + \sigma_s^2)) = \exp(-v_i^2/2\sigma_{Lo}^2(CNR + 1)) = P_{FA}^{(CNR+1)^{-1}} \quad (17)$$

The same result occurs for square-law device detection.

### 4.1 Independent Range Cell Detections

Because there are 14 nearly independent coherent source cells on the TMD diffuse cylinder target at the assumed  $45^\circ$  aspect, we have 14 nearly independent measurements, and the probability of one or more threshold crossing detections out of n is given by:

$$P_D(\geq m \text{ of } n) = \sum_{x=m}^n \frac{n!}{x! (n-x)!} P_D^x (1-P_D)^{n-x} \quad (18)$$

with  $m = 1$  and  $n = 14$ . From equation (18) we find that we need a per range cell  $P_D$  of 0.15 to achieve an 0.9  $P_D$  for all the 14 range cells. From equation (17) we also find that we require a CNR of about 4 per source region on the target.

For the NMD cone target of roughly 7 cells, from equation (18) we find we need a per range cell  $P_D$  of 0.28 to achieve an 0.9  $P_D$  for 7 cells. From equation (17) we find we require a CNR of about 6 per cell at a  $10^{-4}$   $P_{FA}$ . We note that this is an improvement with respect to unresolved target detection (1 range bin).

### 5.0 Speckle Modulation Effects

The diffuse target surface roughness produces constructive and destructive interference effects known as laser speckle. The dominant speckle modulation effects are reviewed here.

(1) **Transverse speckle lobe motion:** The maximum velocity spread from a rotating cylinder is

$$\Delta V_{total \text{ spread}} = \omega D \sin(\theta) \quad (19)$$

and, therefore, the total Doppler spread from a rotating cylinder is given by



$$\Delta f_{total} = 2\omega D \sin(\theta)/\lambda \quad (20)$$

The average speckle size back at the transmitter/receiver is

$$\begin{aligned} \langle d_{speckle 1} \rangle &= \frac{\lambda R}{D} \approx 4m, \\ \langle d_{speckle 2} \rangle &= \frac{\lambda R}{L \sin(\theta)} \approx 0.6m \end{aligned} \quad (21)$$

at 11.15  $\mu m$  for a nominal 1 m diameter, 10 m long cylinder at 45°. The speckle velocity perpendicular to the axis of rotation is given by

$$V_{speckle 1} = 2\omega R \sin(\theta) \quad (22)$$

and the transit time over the aperture is approximately

$$\tau_{transit} = \frac{\langle d_{speckle 1} \rangle}{V_{speckle 1}} = \frac{\lambda}{2D\omega \sin(\theta)} = \frac{1}{\Delta f_{total}} \approx 18 \mu s \quad (23)$$

from equation (21) for nominal targets of interest.

(2) The rotation of **new random phase scatter points** on the cylinder's surface into the ladar FOV results in a new speckle realization. This determines a target coherence time,  $\tau_{exchg}$ , due to "speckle exchange." George<sup>11</sup> has shown that the cylinder scatter-point-exchange coherence time is given by

$$\tau_{exchg} = 4 \sqrt{\frac{D}{2\lambda}} \tau_{trans} = \frac{\sqrt{8\lambda/D}}{\omega \sin(\theta)} \approx 32 ms \quad (24)$$

which is considerably shorter than a  $\pi/2$  rotation period. We also assume here that pitch and yaw rates are much smaller than the roll rotation rate.

## 6.0 Range-Doppler Image Signal Processing

We assume for this analysis that the local-oscillator-laser is set in frequency to bring the received Doppler shifted laser light down to an intermediate frequency (IF) of roughly 500 MHz with a bandwidth of  $\pm 162.5$  MHz at the detector output (single-phase). This spectrum is shown in **Figure 4** where the 2.9 ns micro-pulse bandwidth is 325 MHz (250 MHz @ -3dB) and the spectral peaks are separated by 1/40 ns or 25 MHz. The signal spectral peaks are  $N_{\mu p}^2$  above that of a single micro-pulse spectrum where  $N_{\mu p}$  is the number of micro-pulses in the train =  $T_{macro} / 40$  ns. This computer run assumes a 15  $\mu s$  macro-pulse, thus, the spectral peaks are 375<sup>2</sup> or 141,000 above that of a single micro-pulse, and the per micro-pulse CNR is 10<sup>-4</sup> or -40dB. Note that

the negative frequency components are the complex conjugate of the positive frequency components for a real (single-phase) signal and are not shown. The detector bandwidth is seen to be 1 GHz from the local-oscillator noise spectrum.

An electrical-LO frequency-locked-loop then brings the 500 MHz IF down to 200 MHz in both inphase and quadrature (I & Q), shown in **Figure 5**. The bandwidth of this mixer stage is assumed to be 500 MHz resulting in very little phase distortion of the signal due to the flat transfer function selected, a 5th-order Butterworth. At this lower center frequency, the signal can be A/D converted at a 2 GS/s sampling rate on both I & Q.

### 6.1 Digital Matched Filter

Next, a digital matched filter (I & Q) is convolved with each 40 ns (80 points @ 2 GS/s) segment in the frequency domain using FFT's<sup>13,14</sup>. This digital matched filter is constructed by sampling the transmitted micro-pulses and constructing an "analytic-function" reference waveform also at the 200 MHz center frequency:

$$V_{ref}^{ANAL} = IFT([1 \ 2 \ 2 \dots 2 \ 2 \ 1 \ 0 \ 0 \dots 0 \ 0] * FT(V_{ref})) \quad (25)$$

where the length of the 0's and 2's is one-half the length of the stored waveform less 1. If we have a perfect laser, the analytic reference may be stored in the computer memory. This nearly perfect analytic-function digital filter produces the spectrum shown in **Figure 6**. We immediately see that the **negative frequency noise components are greatly reduced**. We thus pick up a factor of 2 (+3dB) in CNR from that calculated in equation (14) which included a 2 in the denominator for positive and negative frequencies. The digital matched filter is perfectly matched to the spectrum of the return from a point source. Monte Carlo simulations from spinning cones and cylinders indicate that the improvement of the analytic-function digital matched filter is actually about a **factor of 4 (+6dB) better** than the top hat spectral models used in the CNR analytical equations. This is particularly true for asymmetric micro-pulses (due to higher-order mode-medium effects) in producing a near perfect spectral filter w.r.t. a top hat analytical filter.

### 6.2 Range-Doppler Image Construction

The outputs of the matched filter are then rearranged in a waterfall plot in sequence, each segment being 40 ns long (**Figure 7**). Zeros are

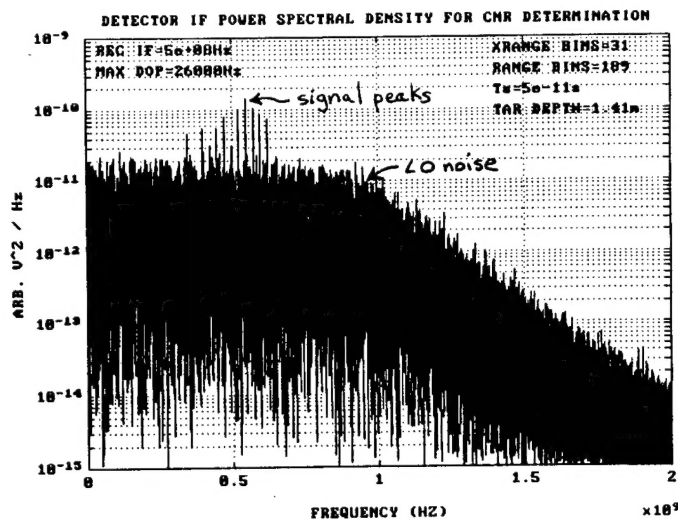


Figure 4. Spectrum of the detector output centered at 500 MHz. CNR =  $10^{-4}$  per micro-pulse.

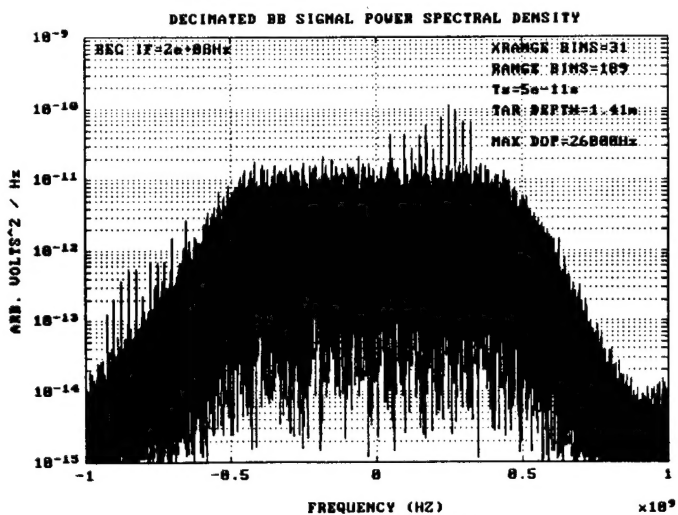


Figure 5. Down shifted (I&Q) spectrum centered at 200 MHz after A/D conversion.

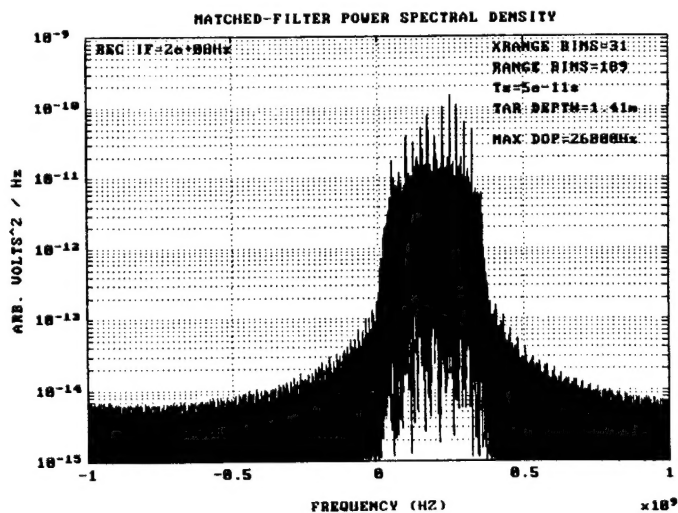


Figure 6. Spectrum of the analytic digital matched filter output. Note the negative frequency noise components are greatly reduced.

added above and below the waterfall sequence prior to FFTing the range bin columns. The number of zeros is determined so that the waveform resolution ( $1/T_{\text{macro}}$ ) subtends at least 4 or 5 FFT points so that triangular or spiked peaks are avoided, and we obtain smooth peaks. For a 40  $\mu\text{s}$  waveform, for example, this would require zero padding to 4096:

$$\frac{1/40\mu\text{s}}{25\text{MHz}/4096} = 4.1 \quad (26)$$

as opposed to zero padding to 2048. FFTing down the columns and taking the magnitude squared is proportional to finding the power spectral density of this range bin. From spectral analysis theory<sup>15</sup> we find the mean square voltage down a range bin column to be

$$\langle v^2 \rangle = \frac{\sum v_i^2}{T_s N_{\text{data}}} = \frac{\sum \Phi_v}{T_s N_{\text{data}}} \quad (27)$$

where the  $v_i$  are the element voltages,  $T_s$  is the sample time,  $N_{\text{data}}$  is the data length ( $N_{\mu p}$ ), and

$$\Phi_v = \frac{T_s}{N_{\text{total}}} FT(v) FT(v)^* \quad (28)$$

is the "periodogram" estimate of a power spectral density (PSD) with  $N_{\text{total}}$  equal to  $N_{\text{data}}$  plus zero padding. Consequently, the average noise PSD in a range-Doppler image column is

$$\langle \Phi_n \rangle = \frac{\langle |v_n|^2 \rangle 40ns N_{\mu p}}{4096} \quad (v^2/\text{Hz}) \quad (29)$$

The average signal PSD is

$$\langle \Phi_s \rangle = \frac{\langle |v_s|^2 \rangle 40ns N_{\mu p}}{(1/T_{\text{macro}})/(25\text{MHz}/4096)} \quad (v^2/\text{Hz}) \quad (30)$$

when the **target bandwidth is less than the waveform resolution**, as the signal is only in a few Doppler bins (the denominator of (30)). Taking the ratio (30) to (29), we find the range-Doppler image column CNR to be

$$CNR_{RD} = N_{\mu p} CNR_{MF} = \frac{T_{\text{macro}}}{40ns} CNR_{MF} \quad (31)$$

when  $T_{\text{coh}} > T_{\text{macro}}$  or  $\delta v_{\text{target}} < 1/T_{\text{macro}}$ . One such range-Doppler image of a 2 m cylinder at 45° is shown in **Figure 8** at a CNR of 5.3 after processing 375 micro-pulses (15  $\mu\text{s}$ ).

When the **target Doppler spread exceeds the waveform frequency resolution**, the target energy gets spread into additional cross-range FFT points. For this situation the average signal PSD in those bins containing signal becomes

$$\langle \Phi_s \rangle = \frac{\langle |v_s|^2 \rangle 40ns N_{\mu p}}{\delta v_{\text{target}}/(25\text{MHz}/4096)} \quad (32)$$

and taking the ratio of (32) to (29)

$$CNR_{RD} = \frac{CNR_{MF}}{40ns \delta v_{\text{target}}} \quad (33)$$

when  $T_{\text{coh}} < T_{\text{macro}}$  or  $\delta v_{\text{target}} > 1/T_{\text{macro}}$ . Thus, the CNR remains **constant** once  $T_{\text{macro}} = 1/\delta v_{\text{target}}$  is reached, since  $\delta v_{\text{target}}$  is fixed. For longer macro-pulse times, non-coherent effects come into play.

### 6.3 Non-coherent Processing of the Range-Resolved Spectra

To further increase the image CNR, we might **non-coherently** sum the range-bin PSDs calculated every  $T_{\text{coh}}$  in a long pulse train. In actuality, the PSD estimator given in equation (28) automatically does this. For example, under the AWACS/EAGLE program<sup>16</sup> it was determined that the TMD targets of interest usually rotate at less than 1/20 revolution per second. This produces a Doppler spread of less than 2 x 28 kHz ( $\text{CO}_2$  wavelengths) at 90° aspect and less than 2 x 19 kHz at the assumed 45° aspect. Due to cylindrical surface weighting, the -3dB Doppler spread is around 19 kHz total, hence, we are limited to macro-pulse lengths of roughly 54  $\mu\text{s}$  (1350 micro-pulses) for efficient coherent signal processing where equation (31) applies. If we select a long pulse train of  $T_{\text{macro}} = 10$  ms, we then have 10 ms / 54  $\mu\text{s} = 185$  independent spectral measurements. If we then non-coherently summed these consecutive independent spectra, we have, from classical microwave radar analysis<sup>17-19</sup>,

$$CNR_{RD\Sigma} = CNR_{MF} \left( \frac{T_{\text{coh}}}{40ns} \right) \left( \frac{T_{\text{macro}}}{T_{\text{coh}}} \right)^{0.7} \quad (34)$$

where the exponent actually varies from 0.6 to 0.8. In the formation of the PSD via equation (28) down each range-bin, that is what happens. This amounts to a factor of up to 52,000 for a 10 ms train and a 54  $\mu\text{s}$  target coherence time. It does, however, require good range-bin and good Doppler-bin tracking (or registration) in order to produce an accurate, unblurred image. We note that retargeting rates of 50 objects per second would allow up to a 20 ms macro-pulse length, further enhancing the summation.

Assuming a 10 ms macro-pulse train of 7.4  $\mu\text{J}$  micro-pulses (185 W average), a 54  $\mu\text{s}$  target coherence time, and a +6dB analytic digital matched filter enhancement, the points where the TMD



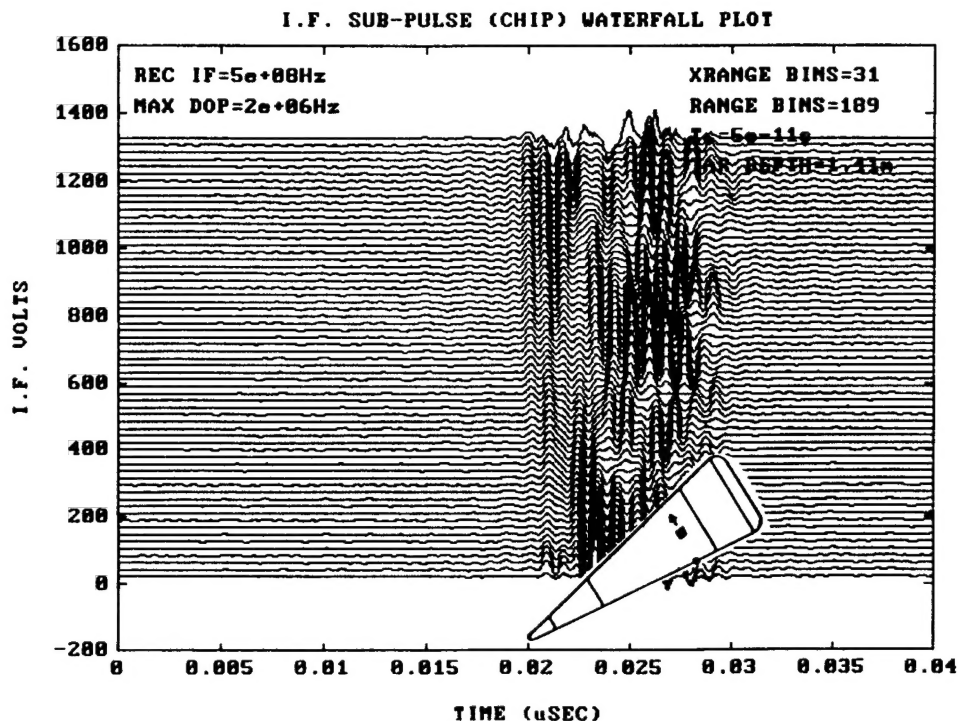


Figure 7. Waterfall plot<sup>14</sup> of the sequence of micro-pulses after matched filtering. Note the slowly varying small signals at the cone tip, and the faster varying strong signals near the base.

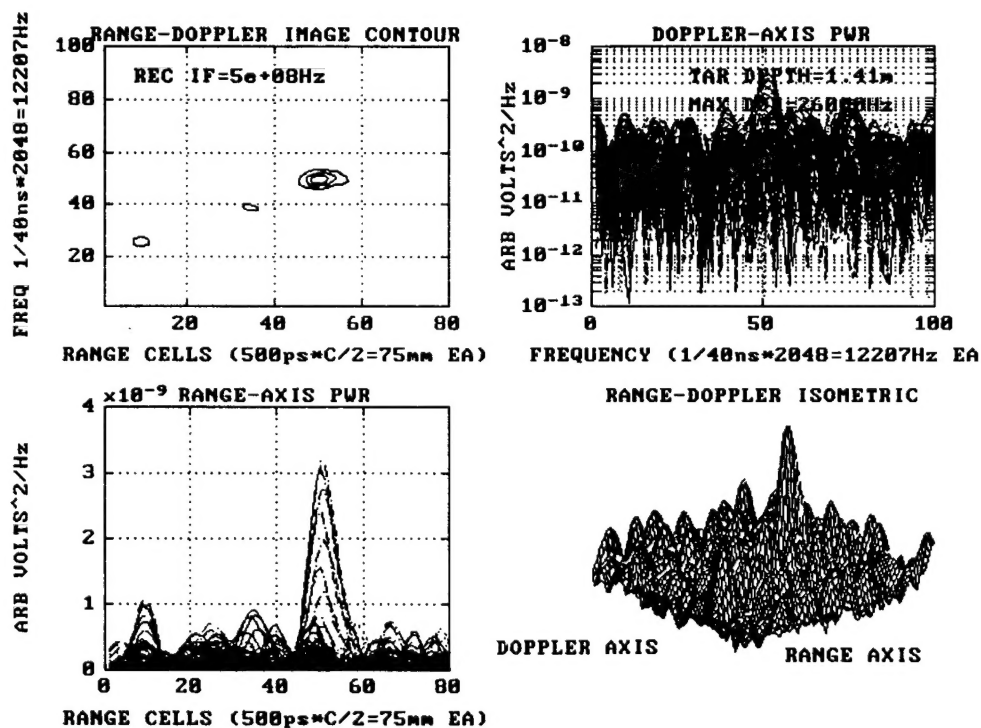


Figure 8. Low CNR range-Doppler image of a cylinder 2 m long at 45° with  $\pm 26$  kHz Doppler spread. Contour, Doppler axis, range axis, and isometric views.  $\text{CNR} = 3.6 \times 10^{-3}$  per micropulse, 5.3 after processing 15  $\mu\text{s}$  (375 micro-pulses) of data. A threshold crossing of the range-axis view is a detection.

$CNR_{RDS}$  reaches 4 are plotted in Figure 9 for various cylinder+cone target altitudes. At the baseline target altitude of 20 km, we see that the per range-cell CNR of 4 is met at 550 km (indicating a full target (14 cells)  $P_D$  of 0.9 at a  $P_{FA} = 10^{-4}$  per Section 4. Atmospheric extinction at low altitudes dominates the losses. For the exo-atmospheric NMD scenario,  $\lambda = 10.6 \mu m$  at  $4 \mu J$  per pulse and we see the  $1/R^4$  dependence in  $CNR_{RDS}$  in Figure 10. Maximum range ( $CNR_{RDS} = 6$ ) occurs at about 370 km with the cone target at  $45^\circ$  aspect.

#### 6.4 Alternative Target Detection Algorithms

Summing down the range columns of the range-Doppler image to form an "amplitude (or amplitude<sup>2</sup>) vs range" image was found to be **not** as effective an algorithm as a range-axis view of the range-Doppler image (magnitude)<sup>2</sup>. This is because the cross-range cells outside the target contain only LO noise and corrupt the cross-range sums. The cross-range bin number must be maintained fairly large to compensate for frequency errors in estimating the target's center of mass Doppler and in the frequency-locked loop. Likewise, summing across the Doppler bins to form a "Doppler resolved target" image is not as good for detection.

#### 7.0 Work in Progress

1) The usual slowly spinning targets do **not** generate Gaussian, Rayleigh, negative-exponential statistics when  $T_{macro} < T_{coh}$ . Monte Carlo runs indicate Rician and modified-Rician (sinewave plus diffuse) statistics are observed with the same  $\langle v_s^2 \rangle$  target signal magnitude but with a reduced variance. This means the **detection statistics will be better**. The allocation of the sinewave component to the diffuse component must be determined as a function of target spin rate such that the total target cross-section sum remains equal to the target true cross-section. The detection of this signal in Gaussian LO noise must then be computed. When  $T_{macro}$  is greater than  $T_{coh}$ , Gaussian, Rayleigh, negative-exponential statistics return.

3) A target aspect angle closer to  $90^\circ$  would probably be more appropriate giving larger signal per range cell.

4) Using the **full** macro-pulse waveform as a digital matched filter and then forming a range-Doppler image (with no Doppler cross-range information) produces a **superior** detection measurement compared to the range-axis view of the

range-Doppler image. The operations per second required for these long vectors may be prohibitive.

5) When there is a range (return time) error, the target image shifts forward and backward in the range-Doppler matrix not causing much of a problem. When there is a center-of-mass frequency error, the peak of the matched filter output decreases and distorts, an effect known as "range-Doppler coupling." The magnitude of this effect is under investigation.

6) Sinusoidal and linear frequency modulation waveforms are being investigated for the endo-atmospheric (ASTP) applications as well.

#### 8.0 Acknowledgements

This work was sponsored under BMDO contract 84-92-C008, Dr. Walter Dyer (TR/TO) program manager and William Thomas and Brian Figie (TRC) DITP and ASTP program managers, respectively. The authors would also like to thank Stephen Kosovac of Computer Sciences, Inc. and the staff of Technology Development Corp., Huntsville for their useful discussions and guidance.

#### References

1. W. Dyer, "Missile Seeker Technology at the Ballistic Missile Defense Organization," AIAA Missile Sciences Conference, Dec. 1996.
2. R. Franklin, et al., "Ladar Technology for Advanced Interceptor Discrimination," AIAA Missile Sciences Conference, Dec. 1996.
3. C. Neumann, J. Paranto, R. Pringle, "Implementation of Target Dynamics into Ladar Radiometric Analysis," Proc. IRIS Active Systems, 1993, Vol. III.
4. S. Kosovac, et al., "Feature Extraction form Range-Resolved Doppler Measurements," Proc. IRIS Active Systems, 1992, Vol. II.
5. J. Paranto, D. Dean, "Overview of Active/Passive System Definition Program," Proc. IRIS Active Systems, 1990, Vol. II.
6. R. Frehlich, M. Kavaya, "Coherent laser radar performance for general atmospheric refractive turbulence," Appl. Opt. 31, 20 Dec. 1991.
7. Klein, Degnan, Appl. Opt., Sept. 1974, p. 2134.
8. H. Yura, "Optimum truncation of a Gaussian beam in the presence of random jitter," JOSA Vol. 12, No.2, Feb. 1995.
9. H. Yura, "LADAR detection statistics in the presence of pointing errors," Appl. Opt. 33, 20 Sept.

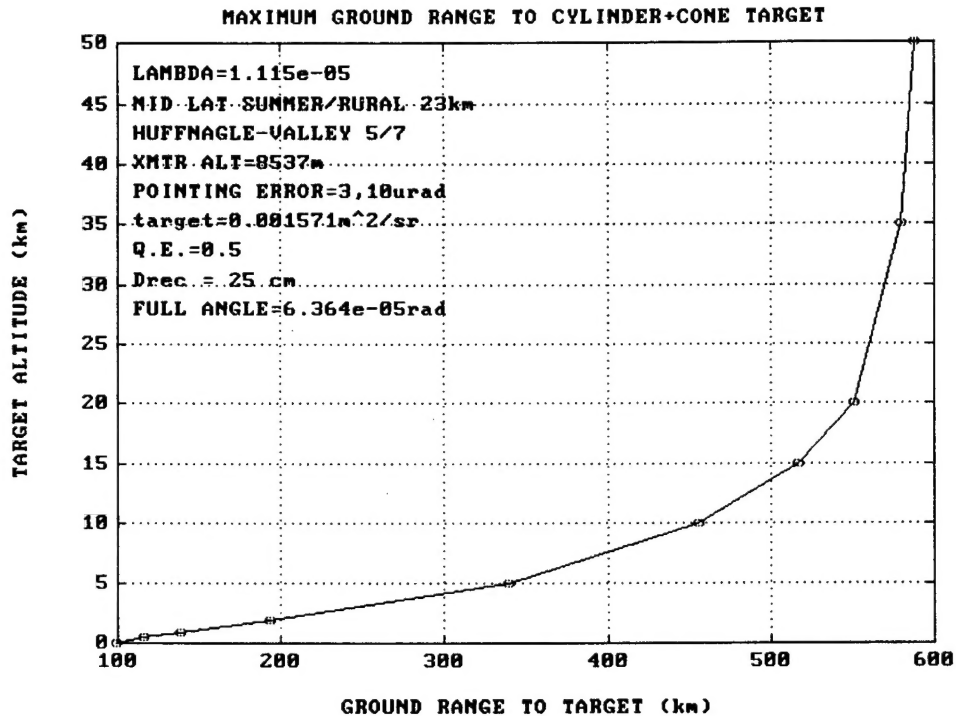


Figure 9. Maximum ground range vs altitude for the TMD cylinder+cone target.  $P_D$  for one or more threshold crossings of 14 range-bins ( $45^\circ$  aspect) is 0.9 at  $10^{-4} P_{FA}$ . The platform altitude is 28,000 feet for this plot.

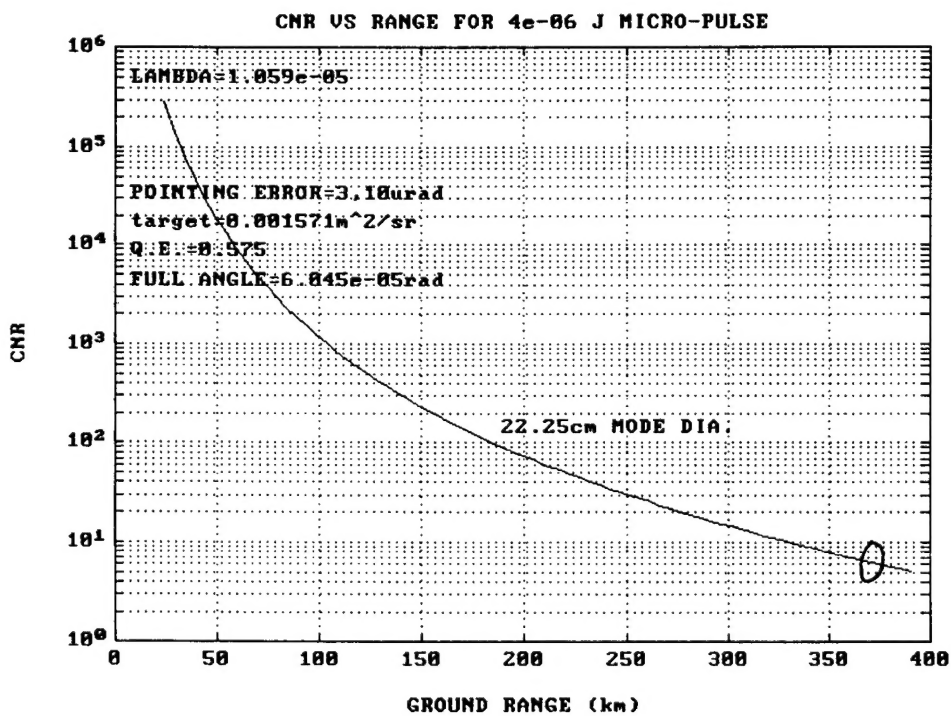


Figure 10.  $CNR_{RDS}$  vs range for the NMD exo-atmospheric cone target. Maximum range for one or more threshold crossings of 7 range-bins ( $CNR = 6$  per bin) is at 370 km.  $\lambda = 10.6 \mu m$ , 4  $\mu J$  pulses.

1994.

10. A. McFarland, et al., *Laser Cross Section Handbook*, Mission Research Corp., WRDC-TR-89-9010.

11. J. Shapiro, B. Capron, R. Harney, "Imaging and target detection with a heterodyne-reception optical radar," *Appl. Opt.*, Vol. 20 No. 19, 1 Oct. 1981.

12. N. George, "Speckle from rough, moving objects," *JOSA*, Vol. 66, Nov. 1976.

13. D. Youmans, et al, "Theoretical and Monte Carlo Analyses of the Range-Doppler Imaging Capabilities of Mode-locked CO<sub>2</sub> Ladars," *SPIE Proc.* Vol. 2702, Gas Laser Technology, Jan. 1996.

14. F. Corbett, et al, "Digital Image Processing System for a High Powered CO<sub>2</sub> Laser Radar," *SPIE Proc.* Vol. 2847, Aug. 1996.

15. R. Fante, *Signal Estimation and Analysis*, John Wiley & Sons, 1988.

16. D. Youmans, D. Fluckiger, "Linear FM chirp pulse compression lidar receiver-operating-characteristic: maximum of M Rayleighs statistics," *SPIE Proc.* Vol. 3065, Laser Radar Technology and Applications II, April 1997.

17. M. Skolnik, *Introduction to Radar Systems*, McGraw Hill, 1980, p. 28.

18. P. Cassady, R. Murata, "Signal processing for coherent laser radar integration of multiple pulses and effects of pointing errors," *SPIE Vol.* 2748, 1996.

19. R. Fante, "Multifrequency Detection of a Slowly Fluctuating Target," *IEEE Trans. AES*, Vol. 32, No. 1, 1996.